GEOLOGICA CARPATHICA, DECEMBER 2016, 67, 6, 509–524 doi: 10.1515/geoca-2016-0032

Surface strain rate colour map of the Tatra Mountains region (Slovakia) based on GNSS data

MARTIN BEDNÁRIK[1], JURAJ PAPČO[2], VLADIMÍR POHÁNKA[1], VLADIMÍR BEZÁK[1], IGOR KOHÚT[1] and LADISLAV BRIMICH[1]

[1] Earth Science Institute, Slovak Academy of Sciences, Dúbravská cesta 9, P.O. Box 106, 840 05 Bratislava, Slovakia; geofmabe@savba.sk
[2] Department of Theoretical Geodesy, Faculty of Civil Engineering, Slovak University of Technology, Radlinského 11, 813 68 Bratislava, Slovakia

(Manuscript received September 29, 2015; accepted in revised form September 22, 2016)

Abstract: The surface deformation of the Tatra Mountains region in Western Carpathians can nowadays be studied directly thanks to precise geodetic measurements using the GNSS. The strain or stress tensor field is, however, a rather complex "data structure" difficult to present legibly and with sufficient resolution in the form of a classical map. A novel and promising approach to the solution of this problem is coding the three principal strain or stress values into the three colour channels (red, green, blue) of an RGB colour. In our previous study, the colour depended on the stress tensor shape descriptors. In the current study, the adapted colouring scheme uses a subset of shape descriptors common to stress and strain, which differ only in the scaling factor. In this manner, we generate the colour map of the surface strain rate field, where the colour of each grid point carries the information about the shape of the strain rate tensor at that point. The resulting strain rate colour map can be displayed simultaneously with the map of the faults or elevations and be easily checked for the data or interpolation method errors and incompatibility with the geophysical and geological expectations.

Keywords: GNSS, surface deformation, tensor field visualization, three-dimensional colour function, Tatra Mountains.

Introduction

Tatra Mountains

The Tatra Mts. (Fig. 1) are the northernmost core mountain range in the arc of the Western Carpathians. Tectonically, they belong to the Inner Western Carpathians (recently reaffirmed by Bezák et al. 2004). Their present-day morphology is a product of the most recent tectonic processes in the Miocene to Quaternary. After the oblique collision of the block of the Inner Carpathians with the European Platform and the subduction of Magura Ocean reached standstill, new tectonic processes initiated in the mantle have led to increased volcanic activity and formation of horst-graben structures, with most horsts uplifted asymmetrically. The asymmetrical uplift of the block of the Tatra Mts. proceeded along the Sub-Tatra fault band (e.g., Nemčok et al. 1994). The Tatra Mts. horst comprises in itself the tectonic units from the previous orogenic periods, mainly the Hercynian and the Palaeoalpine. In the Hercynian period, crystalline units (metamorphics and granitoids) were formed. During the Palaeoalpine Cretaceous period, the superficial nappes of Mesozoic complexes were formed, preserved now mainly on the northern side of the Západné and Vysoké Tatry Mts. and in the Belianske Tatry Mts. A detailed view of the geology of the Tatra Mts. is given by Nemčok et al. (1993). The Neoalpine to recent tectonics of the Tatra Mts. have been studied by, for example, Sperner & Ratschbacher (1995), Burchart (1972), and recently by Králiková et al. (2014). A valuable summary of the research related to the exhumation of the Tatra Mts. can be found in the introductory chapter of Anczkiewicz et al. (2015).

Deformation measurements in the Western Carpathians and Pannonian Basin

The completely blank space of Slovakia on the World Stress Map (WSM) compiled by Heidbach et al. (2009) represents the reluctance of the local researchers to contribute to the WSM rather than a total lack of any research. The early history of stress/strain field research in Western Carpathians and Pannonian Basin definitely includes the extensometric measurements. A summary of their results can be found in Mentes (2008). Their spatial resolution is very low (only five extensometric stations for the whole area of interest) and they only give the projection of the strain tensor at a site usually into one, exceptionally two approximately perpendicular horizontal directions. As the extensometric measurements are sampled frequently enough in time, they could be able to detect sudden tectonic stress changes at the site. Nevertheless, due to the environmental influences (change of temperature, precipitation etc.), they never did so with sufficiently high reliability.

Another category of strain measurement devices frequently used in Central Europe is the dilatometers (crack gauges), especially the mechano-optical ones of the type TM-71 (Košťák 1969). These register the relative motion (in all its

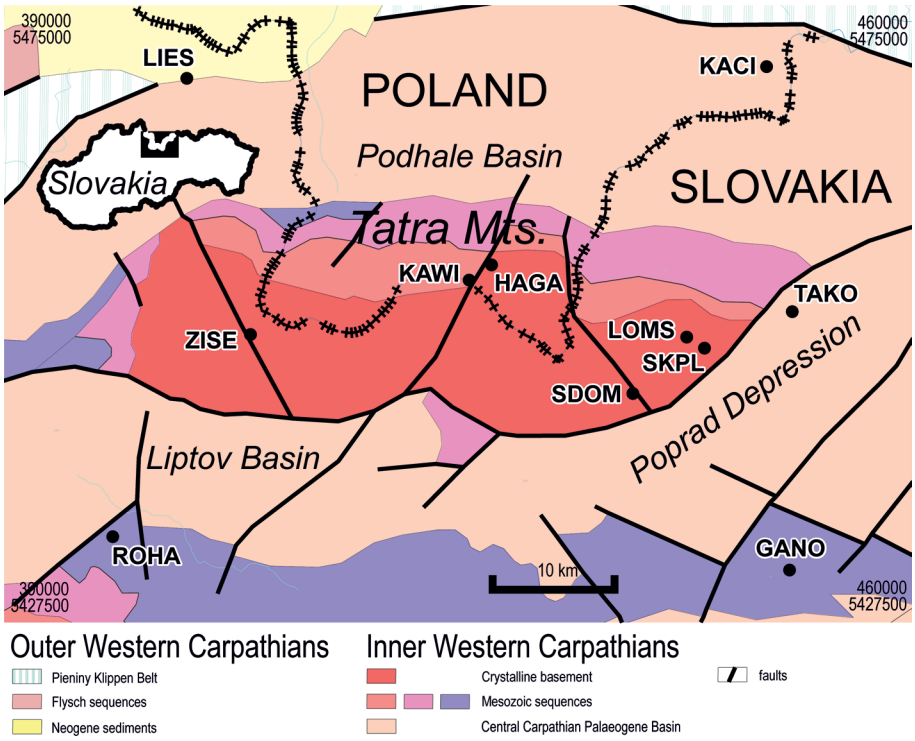

Fig. 1. Tectonic scheme of the Tatra Mts. region based on Bezák et al. (2008). The coordinates [m] of its corners are given in UTM Zone 34 North reference system. In the upper left corner, the overview map of Slovakia shows the studied area with a black rectangle.

degrees of freedom) of two blocks of rock across the crack that separates them. The favourite installation sites are the underground cavities of caves or mine galleries (e.g., Briestenský 2008; Briestenský & Stemberk 2008), thus giving a rise to a new branch of active tectonics research (Littva et al. 2015).

A study by Fojtíková et al. (2010) relates the focal mechanisms of the local earthquakes to the stress field in the Malé Karpaty Mts. Given the number and spatial configuration of seismometers needed to determine the focal mechanisms of many local events, and the uneven spatial and temporal distribution of seismic activity in the Western Carpathians, we cannot hope that any larger portions of Western Carpathians will ever be surveyed in this manner.

With the onset of new technologies, much effort is exerted to measure the surface movements directly. The comprehensive dissertation of Papčo (2010) directly applies to the same geographic region of interest as this paper. The data output of the study serves as our source data. Our method provides a further enhancement of their geophysical readability and interpretability. As Papčo's dissertation is not widely available, in the next chapter, we give a short summary focusing on information relevant to this paper.

GNSS measurements in the Tatra Mountains region

Global navigation satellite systems (GNSS) can be used as very efficient tools for monitoring the velocity of lithospheric plates, including the inner plate motions.

The Tatra Mountains region has attracted the specialists in geodetic monitoring since the early 1980-s. The pioneering work has been done by Hradilek with his high precision classical geodetic measurements (Hradilek 1984). The modern period of this long-term activity started in 1997 within the project CERGOP (Czarnecki & Mojzeš 2000) and CERGOP2-Environment (Fejes 2002) by establishing the special GNSS geodynamics network TATRY. The whole network consists of 30 points, which can be divided into two main groups: primary geodynamics points (18 sites), and the rest of the network dedicated to other research purposes (e.g., local gravity field modelling). Geodynamics points are located in the highest alpine parts (points ZISE (Žiarske sedlo), KAWI (Kasprowy Wierch), PRSO (Predné Solisko) and LOMS (Lomnický štít)), valley parts (points ZICH (Žiarska chata), HAGA (Hala Gąsienicowa), TIDO (Tichá dolina), BIEL (Bielovodská dolina), SDOM (Sliezsky dom), HREB (Hrebienok), SKPL (Skalnaté pleso) and TAKO (Tatranská kotlina)), and 6 points are situated outside the main area (GANO (Gánovce), ROHA (Roháčka, near Liptovský Mikuláš), LIES (Liesek), KACI (Kacwin), RWOO (Rolów Wierch) and GUBA (Gubałówka)). Precise epochal GNSS measurements have been performed annually since 1998 with the durations of approximately 96 hours. Processing was done in the Bernese software version 5.0 (Dach et al. 2007) in accordance with the EPN and CEGRN recommendations (Stangl 2007) using precise IGS orbits, EOP parameters (IGS 2016), absolute GNSS antenna phase centre information and Niell mapping function for the tropospheric delay modelling. All campaigns (from 1998 to 2008) were processed in the ITRS global coordinate system. Connection to ITRF2005 (Altamimi et al. 2007) was established by using the surrounding permanent GNSS stations of EPN: BOR1, GOPE, GRAZ, JOZE and PENC (EPN 2016).

Final coordinates and velocities of the points (in ITRS global coordinate system) were estimated in the special program COMB_NET, which was designed for combinations of networks taking into account the time epoch (Hefty 2004; Hefty & Gerhátová 2006). The inner plate velocities were derived from the Eurasia lithospheric plate velocity model APKIM2005D (Drewes 2009).

The horizontal velocities reach up to 2 mm/year, but at the majority of the points they are below 1 mm/year (cf. Appendix; Fig. 2). Vertical velocities of the points are very unstable and

problematic, because none of them surpasses its uncertainty and they show very variable trends. Next analysis and strain field determination were performed without the points with problematic behaviour (BIEL, ZICH, TIDO, PRSO, GUBA, RWOO and HREB). The main reasons for these exclusions were locations of the points (sites affected by landslide or moraine movements), character and magnitude of the velocity, sudden jumps in the time series or shorter measurement period.

For the purposes of this paper, two more stations — GANO and LIES — were excluded from the dataset based on considerations about the sites' geological settings. GANO can be influenced by slope motions. LIES is located on Neogene sediments. TAKO, situated on glaciofluvial deposits, has been kept in the dataset. The difference is that the contribution of TAKO to the interpolation function can be corrected by contributions of the neighbouring stations (and it has also a lower weight in the weighted least squares due to its higher standard deviation of velocity), whereas LIES is a stand-alone site that would influence a broader area.

Methods

Interpolation methods

The main task is to produce a colour map of the surface strain rate tensor field. The strain rate tensor contains the spatial derivatives of the surface velocity field. In Cartesian coordinates and index notation

$$\dot{\varepsilon}_{jl} = \left(\dot{u}_{j,l} + \dot{u}_{l,j}\right)/2 . \quad (1)$$

The dot over the symbols denotes the first time-derivative of strain and displacement. The indices after the comma denote partial derivatives with respect to the l-th or j-th spatial coordinate.

Of that velocity field $\dot{u}_j$, we have available only a few samples — the horizontal surface velocities measured at the stations. From those samples, taking into account their errors, we have to interpolate the horizontal velocity field covering the whole region. The interpolated velocity field can be specified in the form of a function formula, which can be differentiated analytically, or as a regular grid of values, which can be differentiated numerically.

At the stations's positions, the exact interpolation methods yield exactly the same values as the respective measured values. This is not very desirable in the situation of known, relatively large data errors. The approximate interpolation methods, which do not adhere to the measured values exactly, should then be preferred. This was also our choice.

The next choice depends on our notion of regional dynamics. A region with a stable crust can be regarded as moving as a whole, with small, regional scale perturbations. In this case, we shall search for a whole region interpolation formula. In a less quiet region, the local dynamics concentrated to the vicinity of faults and other active structures may locally prevail over the regional trends. In the latter case, the local interpolation methods, effectively taking into account only the nearest stations, may be a better choice. An increase of the (polynomial) order of the whole region interpolation formula could have a seemingly similar effect of capturing the local behaviour. Nevertheless, this solution has many side effects. The worst of them is a better adherence to the values measured at the sites at the expense of very unsatisfactory behaviour elsewhere in the region. Increasing the order of approximation makes more sense in the local interpolation methods.

We tested both the whole region least squares interpolations, implemented in a script written in Mathematica 9 by Wolfram Research, and the local moving least squares interpolation (Pohánka 2005), implemented in a stand-alone program.

In the whole region weighted least squares interpolation under Mathematica 9 we took advantage of the built-in Minimize[ ] function to find the values of the coefficients c_{mn} of the polynomial

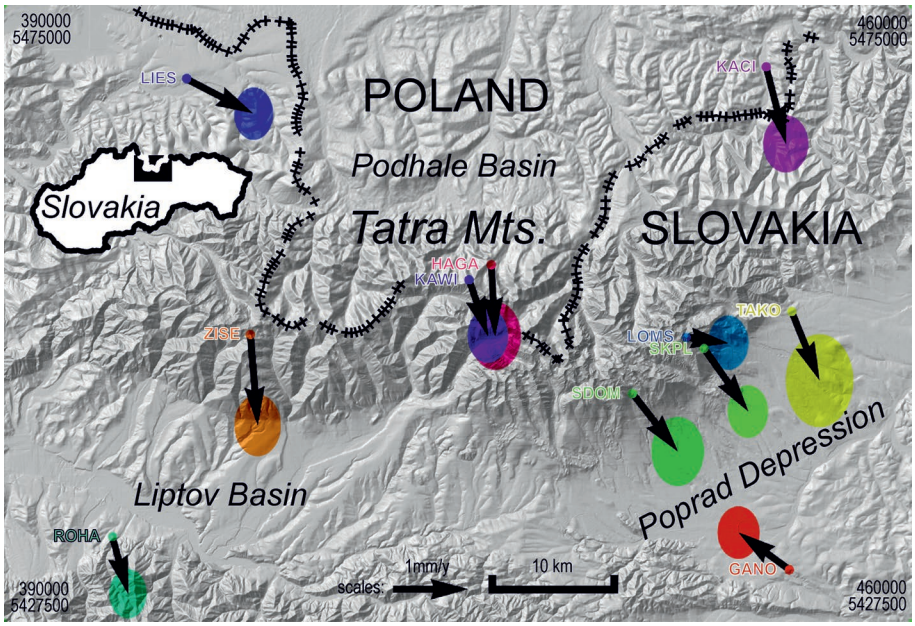

Fig. 2. Measured surface velocities (arrows) and their standard deviations (ellipses) within the area of interest with an extent of 70×47.5 km² (the coordinates [m] of its corners are given in UTM Zone 34 North reference system). Here, the different colours are used only as a graphical tie between the measurement site and the standard deviation of velocity at the site. In the upper left corner, the overview map of Slovakia shows the studied area by black rectangle.

$$v^I(x,y)=\sum_{m=0}^{M}\sum_{n=0}^{N}c_{mn}\,x^m y^n \qquad (2)$$

that yield the minimum of $\sum_k w_k\left|v_k^I-v_k^O\right|^2$, where $v_k^I=v^I(x_k,y_k)$ is the interpolated value and v_k^O is the value observed at the site (x_k, y_k) and w_k, $w_k>0$, are the weights at the sites. $v^I(x, y)$ stands for any of the horizontal surface velocity components. In our implementation, the weights of the approximation errors are proportional to the reciprocals of the specified standard deviations of the measured velocity values at the sites. Thus, the smaller the standard deviation, namely the more reliable the value, the greater weight is attributed to the site. The site's weight could also involve a station's geodynamical reliability factor based on an expert's assessment of the station's geological setting. For instance, the stations on unconsolidated sediments could get a lower rating. We did not, however, implement the station's rating. We instead excluded the problematic stations GANO and LIES from the dataset. The weights based on standard deviations did not have a very significant influence on the results, as the standard deviations vary from site to site only moderately (with an exception of TAKO — cf. Fig. 2) and the almost equal weights did not favour any of the stations.

Our iterative least squares algorithm with adaptive weights yielded interesting results. Its basic idea is simple: if the approximation error $\left|v_k^I(i)-v_k^O\right|$ in the i-th step at the k-th site exceeds the standard deviation δ_k (here we deviate from the usual notation of standard deviation by σ_k, as this symbol denotes principal stress value elsewhere in the paper), then in the i+1-th step the site's weight $w_k(i+1)$ should be increased by the factor of

$$a_k(i)=\left|v_k^I(i)-v_k^O\right|/\delta_k \qquad (3)$$

to

$$w_k(i+1)=a_k(i)\,w_k(i) \qquad (4)$$

in order to reach a more favourable $a_k(i+1)$ ratio (i.e. a lesser exceedance) in the i+1-th step of weighted least squares approximation. In this manner, the weights of all sites shall be iteratively adapted. The iteration process stops when for all sites $\left|v_k^I(i+1)-v_k^O\right|\doteq\left|v_k^I(i)-v_k^O\right|$. The observed convergence of the process was rather slow (up to hundred iterations needed) and very moderately uneven. It seems to be, however, independent of the initial weights $w_k(0)$. We tried $w_k(0)=1$ as well as $w_k(0)=\delta_k^{-1}$.

Let us denote $v_k^{IA}=\lim_{i\to\infty}v_k^I(i)$. The adaptive weights algorithm tends to minimize the maximum approximation error $\max_k\left|v_k^{IA}-v_k^O\right|$ reached within the dataset, whereas the original least squares approximation directly minimizes $\sum_k w_k\left|v_k^I-v_k^O\right|^2$. Interestingly, the Mathematica's Minimize[ ] function was unable to find the global minimum of $\max_k\left|v_k^I-v_k^O\right|$ directly. The detour through iterative least squares is a necessity.

The moving least squares interpolation formula in the version of Pohánka (2005) is the simplest possible function that meets a set of basic requirements that an interpolation function has to fulfil. The polynomial in local coordinates around the point whose value it has to interpolate should be preferably of the second order. The weights of the squared interpolation errors at the measurement sites decrease with the distance to the interpolation point. The behaviour of the function can be controlled by two parameters: the smoothing distance d_0 and the regularization distance d_1.

From stress to strain colouring

The choice of the tensor field visualization method depends on how much we want to show in order to be understood, as well. Some methods require from the reader of the visualized tensor field a sufficiently deep understanding of the tensor notion and nature, or a superb 3D spatial imagination and orientation, which can be a quite high expectation for some users. A simple single-indexed colouring of stress states, whose typical geophysical application is the WSM (Heidbach et al. 2009), is on the other end of the stress state visualization methods' spectrum. Bada et al. (2007) goes one step further and interpolates the discrete colours attributed to the stress state points into a continuous stress state colour map. The less colours the stress mapper has available, the more industrious (s)he has to be in design of the glyphs for coding the stress states. Still, a greyscale stress map remains a big challenge for the reader (Jarosiński et al. 2006).

Our stress colouring method, described in Bednárik & Kohút (2012) in detail, and now adapted to colouring strains as well, aims to produce a reader-friendly, yet information-loaded colour map of a stress or strain field. The stress or strain colour map however differs from the standard colour map of a scalar quantity like height or temperature in one important aspect: our colours depend on three scalar quantities (the three principal stress or strain values) at once.

The stress tensor colouring method introduced in Bednárik & Kohút (2012) needs an adjustment to the current application. The main challenge is the unavailability of the relevant rock characteristics (elastic and rheological parameters, material strength, planes of weakness etc.) at the computation points. In a complex geological environment to be expected in the Tatra region, the stress field is influenced by many variously oriented faults, some well exposed and documented, some unknown. In this situation, the construction of a surface stress field would be a too daring enterprise. Instead, we rather opted for adaptation of the original method to the colouring of the surface strain rate tensor field.

For the sake of derivation of the formulae, let us start with the simplest isotropic elastic model. Here, the Hooke's law in Cartesian coordinates has the form

$$\begin{pmatrix}\sigma_{11}\\ \sigma_{22}\\ \sigma_{33}\\ \sigma_{23}\\ \sigma_{31}\\ \sigma_{12}\end{pmatrix}=\begin{pmatrix}\lambda+2\mu & \lambda & \lambda & 0 & 0 & 0\\ & \lambda+2\mu & \lambda & 0 & 0 & 0\\ & & \lambda+2\mu & 0 & 0 & 0\\ & & & \mu & 0 & 0\\ & & & & \mu & 0\\ & & & & & \mu\end{pmatrix}\begin{pmatrix}\varepsilon_{11}\\ \varepsilon_{22}\\ \varepsilon_{33}\\ 2\varepsilon_{23}\\ 2\varepsilon_{31}\\ 2\varepsilon_{12}\end{pmatrix}, \qquad (5)$$

where λ and μ are the Lamé elastic parameters at the point. The symmetrical lower diagonal part of the stiffness matrix has been omitted.

Our original colouring method was based on transforming the principal stress values into so called colourables *D, M, A* or their rescaled values *d, m, a*. We are interested to see whether similar colouring can be done with the principal strains. The first to be noted consequence of the isotropic Hooke's law (5) is that the principal stress directions and the principal strain directions in isotropic elastic model are coaxial (we leave the proof to the reader).

Let us have an isotropic elastic halfspace limited by a horizontal free surface. Within the surface, let us introduce the horizontal coordinate axes and denote them $\mathbf{e}_1$, $\mathbf{e}_2$. The remaining coordinate axis $\mathbf{e}_3$ will be vertical. If the horizontal surface is traction-free, then $\sigma_{33}=0$, $\sigma_{23}=0$, $\sigma_{31}=0$, and the relationship of the relevant stresses and strains degenerates to a 2D case (called plane stress state), described by the matrix equation

$$\begin{pmatrix}\sigma_{11}\\ \sigma_{22}\\ \sigma_{12}\end{pmatrix}=\begin{pmatrix}4\mu(\lambda+\mu)/(\lambda+2\mu) & 2\lambda\mu/(\lambda+2\mu) & 0\\ 2\lambda\mu/(\lambda+2\mu) & 4\mu(\lambda+\mu)/(\lambda+2\mu) & 0\\ 0 & 0 & \mu\end{pmatrix}\begin{pmatrix}\varepsilon_{11}\\ \varepsilon_{22}\\ 2\varepsilon_{12}\end{pmatrix}, \tag{6}$$

or, after the substitution of $\lambda=\dfrac{\nu E}{(1+\nu)(1-2\nu)}$, $\mu=\dfrac{E}{2(1+\nu)}$, where E is the Young's modulus and ν is the Poisson's constant

$$\begin{pmatrix}\sigma_{11}\\ \sigma_{22}\\ \sigma_{12}\end{pmatrix}=\frac{E}{1-\nu^2}\begin{pmatrix}1 & \nu & 0\\ \nu & 1 & 0\\ 0 & 0 & (1-\nu)/2\end{pmatrix}\begin{pmatrix}\varepsilon_{11}\\ \varepsilon_{22}\\ 2\varepsilon_{12}\end{pmatrix}. \tag{7}$$

It is obvious that two of the principal stress and strain directions are horizontal (generally not equal to $\mathbf{e}_1$, $\mathbf{e}_2$) and the third is vertical i.e. equal to $\mathbf{e}_3$. Let us adopt the notation σ_1, σ_2 (ε_1, ε_2) for horizontal principal stresses (strains) and σ_3 (ε_3) for the vertical principal stress (strain). Henceforth we completely abandon the widely used convention of sorting and indexing the principal stresses and strains according to their size. At the horizontal traction-free surface, the principal stress value σ_3 corresponding to the vertical principal direction equals to zero. This assumption is valid for any constitutive model.

In the isotropic elastic case, one of the principal directions of strain is vertical, as well as with stress. Nevertheless, the vertical principal strain value ε_3 is in general non-zero:

$$\varepsilon_3=-\lambda(\varepsilon_1+\varepsilon_2)/(\lambda+2\mu)=-\nu(\varepsilon_1+\varepsilon_2)/(1-\nu). \tag{8}$$

After some algebra, we discover two useful relationships between the principal stress and the principal strain values valid in the case of plane stress:

$$\sigma_m=(\sigma_1+\sigma_2)/2=(\varepsilon_1+\varepsilon_2)\mu(3\lambda+2\mu)/(\lambda+2\mu)=E(\varepsilon_1+\varepsilon_2)/(2(1-\nu)), \tag{9}$$

$$\tau_m=(\sigma_1-\sigma_2)/2=\mu(\varepsilon_1-\varepsilon_2)=E(\varepsilon_1-\varepsilon_2)/(2(1+\nu)). \tag{10}$$

The horizontal mean stress σ_m and the horizontal maximum shear stress τ_m are the basic stress tensor shape descriptors in the case of plane stress (or plane strain) or can be combined to produce some more advanced shape descriptors — for instance the descriptor (15).

The dependence of ε_3 on ε_1, ε_2 (8) as well as the reducibility of the plane stress state to a 2D horizontal problem (6), (7) are very welcome facts to us. Having in mind the large error of the vertical GNSS velocity component, confirmed also by Papčo (2010) during his field experiments in the Tatra Mts., we can now discard the vertical GNSS data and take into account only the horizontal velocity components and compute the horizontal 2D strain or stress rate tensor. The eigenvalues $\dot{\varepsilon}_1$, $\dot{\varepsilon}_2$ ($\dot{\sigma}_1$, $\dot{\sigma}_2$) can then be completed by $\dot{\varepsilon}_3$ ($\dot{\sigma}_3$) to the full 3D strain or stress rate state.

Let us seek all colourable stress tensor descriptors as functions f with the property

$$f(\sigma_1,\sigma_2,\sigma_3)=C\,f(\varepsilon_1,\varepsilon_2,\varepsilon_3), \tag{11}$$

where C is a scaling factor. The scaling factor will then be eliminated in the process of rescaling the output range of f to the interval $\langle -1,1\rangle$. Thus, the procedures for computing such tensor characteristics will stay the same and will yield exactly the same colours, whether applied to principal stresses or strains. Most importantly, the strain states can be coloured without (almost) any knowledge of material parameters, which is our goal.

We immediately realize that the descriptors σ_m (9), τ_m (10) have exactly the desired form (11). The maximum shear stress τ_m is the quantity upon which is based the Tresca criterion, not the most appropriate to be used for the brittle surface of the Earth's crust. The problem with the more realistic Mohr-Coulomb criterion

$$D_c=|\tau_m|-(S_0\cos\phi+\sigma_m\sin\phi) \tag{12}$$

whether describing the failure on nascent or pre-existing faults, is that it cannot be factorized like (11). Thus, the Mohr-Coulomb (unlike the Tresca) criterion D_c cannot be used for colouring of strain states without the knowledge of the relevant material parameters. We have to be satisfied with the strain-compatible Tresca criterion as a rough indicator D of the proneness to failure (a not very different alternative could be the von Mises yield criterion).

In the plane stress case at the surface, the vertical principal stress always equal to zero narrows the range of the values, that the relevant mean stress σ_m controlling the fault friction in the Mohr-Coulomb criterion (12) can take, to the vicinity of zero. With σ_m not far from 0, the difference of the Tresca or von Mises criterion and the Mohr-Coulomb criterion becomes less dramatic and the Tresca (or von Mises) criterion becomes an acceptable option.

The last step in computing the first colourable d is the normalization of $D\in\langle D_{\min}, D_{\max}\rangle$ to $d\in\langle -1,1\rangle$:

$$d=\begin{cases} 0 & \text{for } D_{\max}=D_{\min} \\ \dfrac{2D-D_{\max}-D_{\min}}{D_{\max}-D_{\min}} & \text{for } D_{\max}\neq D_{\min} \end{cases}, \qquad (13)$$

where $D=\mu\max\left(|\varepsilon_1-\varepsilon_2|,|\varepsilon_1-\varepsilon_3|,|\varepsilon_2-\varepsilon_3|\right)$ (Tresca failure criterion used), and $D_{\max}$, $D_{\min}$ are the maximum and minimum of D to be shown.

The best candidate for the colourable M, indicating whether the stress/strain state is compressive or tensile, is the mean of the horizontal principal stresses/strains σ_m (9). The normalization of $M\in\langle M_{\min}, M_{\max}\rangle$ to $m\in\langle-1,1\rangle$ is analogical to (13):

$$m=\pm\begin{cases} 0 & \text{for } M_{\max}=M_{\min} \\ \dfrac{2M-M_{\max}-M_{\min}}{M_{\max}-M_{\min}} & \text{for } M_{\max}\neq M_{\min} \end{cases}, \qquad (14)$$

where $M=\sigma_m$, and $M_{\max}$, $M_{\min}$ are the maximum and minimum of M to be shown. Like in (13), $M_{\max}$, $M_{\min}$ do not need to be the actual extrema of M within the investigated region. In that case, however, colours generated for $M>M_{\max}$ or $M<M_{\min}$ are the same as the colours for $M=M_{\max}$ or $M=M_{\min}$, respectively — the palette used in the map becomes saturated.

Unlike in (13), it is convenient to map $M=0$ to $m=0$. To assure this, $M_{\min}$ has to be set to $M_{\min}=-M_{\max}$ (or $M_{\max}$ to $M_{\max}=-M_{\min}$). With the ± switch we added the possibility to invert the scale.

The last colourable A (rescaled to a) shall be a predictor of the fault orientation. In its original form (Bednárik & Kohút 2012), a has not made a clear colour distinction between the regions with different orientations of the theoretical fault plane. Here we propose the solutions. Let us show the fault planes, whose normal vector has the vertical component equal to zero by cold colours and all other fault planes by warm colours (or vice versa). If $\sigma_1<\sigma_3<\sigma_2$ or $\sigma_2<\sigma_3<\sigma_1$, the stress state would favour the horizontal strike-slips on fault planes, whose normal vectors are horizontal. Here once again, we take advantage of $\sigma_3=0$. Then, $|\tau_m|>|\sigma_m|$ means that the horizontal principal stresses σ_1, σ_2 have different signs and $\sigma_3=0$ falls between them. Thus,

$$A=|\tau_m|/|\sigma_m|=\frac{|\varepsilon_1-\varepsilon_2|(\lambda+2\mu)}{|\varepsilon_1+\varepsilon_2|(3\lambda+2\mu)}=\frac{|\varepsilon_1-\varepsilon_2|(1-\nu)}{|\varepsilon_1+\varepsilon_2|(1+\nu)} \qquad (15)$$

is a suitable indicator of the fault orientation, because it also meets the condition (11). One complication arises from the need to map the output range of A to $\langle-1,1\rangle$, the other from the fact that a fault orientation indicator has to be scaled locally, depending only on the strain eigenvalues at the point. The scaling factor $(1-\nu)/(1+\nu)$ cannot be eliminated by the normalization over the whole region, unlike in the case of D or M. The only way to eliminate the scaling factor is to estimate it based on the estimate of the Poisson's constant. Fortunately, its variations in the relevant crustal rocks are not large in relation to the goals of this study. The value of the scaling factor can be guessed and eliminated with sufficient accuracy.

An elegant way to map $A\in\langle0,\infty)$ in (15) to $A^{log}\in(-\infty,\infty)$ and $A=1$ to $A^{log}=0$ is to take the logarithm (of any suitable base b)

$$A^{\log}=\pm\log_b\frac{|\tau_m|}{|\sigma_m|}=\pm\left(\log_b\frac{|\varepsilon_1-\varepsilon_2|}{|\varepsilon_1+\varepsilon_2|}+\log_b\frac{(1-\nu)}{(1+\nu)}\right) \qquad (16)$$

and normalize subsequently to $a\in\langle-1,1\rangle$ (similarly to (14)), with the option to cut off the extreme values. In real data, we almost never hit the singularities of A or A^{log}, nevertheless, we have to prevent the overflows. With the ± switch we added the possibility to invert the scale, just as in the case of m.

We can offer a different and more general solution to the fault plane descriptor of the class (11). The term

$$|\sigma_1-\sigma_2|/\left(|\sigma_1-\sigma_3|+|\sigma_3-\sigma_2|\right) \qquad (17)$$

is singular for the hydrostatic stress state $\sigma_1=\sigma_2=\sigma_3$. In all other cases it evaluates to 1, if the vertical principal stress value σ_3 falls between the horizontal eigenvalues σ_1 and σ_2 (or is equal to either of the two), otherwise yields a value from the range $\langle0,1)$. Since we want to have a colour gradation in the first case, as well, and want to cover the whole output range $a\in\langle-1,1\rangle$, we define a as a forked function

$$a=\pm\begin{cases} \dfrac{\sigma_3-\sigma_2}{\sigma_1-\sigma_2} & \text{for } \dfrac{|\sigma_1-\sigma_2|}{|\sigma_1-\sigma_3|+|\sigma_3-\sigma_2|}=1 \\ \dfrac{|\sigma_1-\sigma_2|}{|\sigma_1-\sigma_3|+|\sigma_3-\sigma_2|}-1 & \text{for } \dfrac{|\sigma_1-\sigma_2|}{|\sigma_1-\sigma_3|+|\sigma_3-\sigma_2|}\neq1 \end{cases}. \qquad (18)$$

The term $(\sigma_3-\sigma_2)/(\sigma_1-\sigma_2)$ in the upper branch is formally identical with the stress shape ratio Φ used in structural geology. The descriptor (18) can be used not only in the case of plane stress on the free surface, as (15), (16), but also in a more general case of $\sigma_3\neq0$, but still considerable as vertical principal stress. In the most general application, from the three principal stress directions, one could be selected as "the most vertical" and the respective principal stress values can be denoted accordingly to comply with the convention behind (18). In favour of the convertibility to the strain formulation, it is also advantageous not to substitute $\sigma_3=0$ even in the case of plane stress. The relationship $(\sigma_i-\sigma_j)/2=\mu(\varepsilon_i-\varepsilon_j)$ is valid for any mutually corresponding couples of stress and strain principal values σ_i, ε_i and σ_j, ε_j (and for $i=j$, as well). Then in terms of strains, (19) is as simple as the original formula in stresses (18):

$$a=\pm\begin{cases} \dfrac{\varepsilon_3-\varepsilon_2}{\varepsilon_1-\varepsilon_2} & \text{for } \dfrac{|\varepsilon_1-\varepsilon_2|}{|\varepsilon_1-\varepsilon_3|+|\varepsilon_3-\varepsilon_2|}=1 \\ \dfrac{|\varepsilon_1-\varepsilon_2|}{|\varepsilon_1-\varepsilon_3|+|\varepsilon_3-\varepsilon_2|}-1 & \text{for } \dfrac{|\varepsilon_1-\varepsilon_2|}{|\varepsilon_1-\varepsilon_3|+|\varepsilon_3-\varepsilon_2|}\neq1 \end{cases}. \qquad (19)$$

The only problem is that in plane stress, $\varepsilon_3 \neq 0$. Thus, the ε_3 given by (8) and involving the Poisson's constant has to be substituted (we leave the task to the reader). Even in this case, we ended up with the necessity to enter a single material parameter, which we wanted to avoid.

At this point, we have two remarks. In $A=|\tau_m|/|\sigma_m|$, we have an obvious example that out of the three tensor descriptors *D, M, A* of the plane stress state, only the first two are independent. This corresponds to the degenerate 2D character of the plane stress state, where only the horizontal principal strain values are independent and the vertical one is their linear combination. In spite of this, the colourable *a* plays an important role in the colour generation. A necessary consequence of the dependence of *A* on *D* and *M* is a somewhat reduced colour space compared to the full colour cube (Fig. 3a,b), which is only a minor flaw. In *a* according to (19), that interdependence of colourables is hidden, but still present.

The other remark applies to the now unveiled fact that expressing the stress tensor descriptors in terms of principal strains is a quite unnatural task. The more the descriptor pertains to the balance of forces — like in the case of Mohr-Coulomb failure criterion or the fault plane preference indicator — the bigger the need for the input of material parameters to convert the strains back to stresses. We tried to keep that need as small as possible, but in the case of *A*, we had to make an exception and admit the Poisson's constant to enter our calculations.

The herewith introduced tensor shape characteristics *D, M, A* and their rescaled values *d, m, a* can be regarded in two different ways: we either take them for stress tensor shape descriptors expressed in terms of principal strains, under the assumption of isotropic elasticity (or some other simple constitutive model); or we completely ignore their stress rootage and any underlying assumptions and take them for independent strain state characteristics. They can then be used as strain rate tensor descriptors, as well.

To generate the colours corresponding to the colourables *d, m, a*, the user can choose from several RGB colour function formulae we constructed:

$$c(d,m,a)=\frac{1}{4}\begin{pmatrix}3+a-d+m+ad+dm-a|m|(1+d)\\3+a-d-m+ad-dm-a|m|(1+d)\\3-a-d-ad\end{pmatrix}^T \quad (20)$$

generates stress colours on white background, where white (1, 1, 1) is associated with minimum Tresca stress ($d=-1$).

$$c^{Blk}(d,m,a)=\frac{1}{4}\begin{pmatrix}1+a+d+m+ad+dm-a|m|(1+d)\\1+a+d-m+ad-dm-a|m|(1+d)\\1-a+d-ad\end{pmatrix}^T \quad (21)$$

generates stress colours on black background, where black (0, 0, 0) is associated with minimum Tresca stress ($d=-1$).

The simpler, however less vivid colours generating trilinear stress colour functions are also available for both backgrounds:

$$c_{lin}(d,m,a)=\frac{1}{4}\begin{pmatrix}3-d+m+dm\\3-d-m-dm\\3-a-d-ad\end{pmatrix}^T, \quad (22)$$

$$c_{lin}^{Blk}(d,m,a)=\frac{1}{4}\begin{pmatrix}1+d+m+dm\\1+d-m-dm\\1-a+d-ad\end{pmatrix}^T. \quad (23)$$

With these settings, we produce a three-dimensional colour palette changing from green to red as the strain/stress state changes from extensional to compressional, from dark (palette (21)) or pale (palette (20)) to bright colours as the strain/stress state gets closer to failure, from warm to cold hues as the theoretical fault planes become more vertical and more strike-slip. In our opinion, this colour convention is quite logical and intuitive.

With a change of sign in (14), (16), (19) we could have produced a palette more similar to the convention of the World Stress Map (where normal fault is red, strike-slip green and thrust fault blue), but we deliberately chose not to do so. One reason is that we wanted to underline the novelty and independence of our colouring method. The other reason is that due to the logic of the hue–saturation–value (HSV) colour system, we are not able to adhere to WSM convention totally, anyway. To avoid the risk of misleading the reader used to the WSM, we rather opted for a completely different colouring scheme.

Colour maps of strain rates

The colour maps presented here need some translation into human speech in order to be fully appreciated. We are able to distinguish by colours the basic tectonic regime categories:

1. warm red — shortening — thrusting;
2. cold red — transpression;
3. blue — vertical strike-slip faulting;
4. cold green — transtension;
5. warm green — extension — normal faulting or vertical tearing.

In the colour maps, these categories should be understood as likely tendencies, not as sharp statements.

Another help for the reader's imagination can be found in the three-dimensional colour palettes corresponding to (20) and (21) (Fig. 3a,b). They will be used for colouring all the maps in this chapter. In the captions to the figures with maps, we will only specify the respective ranges of *D, M, A* that were normalized to $d\in\langle-1,1\rangle$, $m\in\langle-1,1\rangle$, $a\in\langle-1,1\rangle$.

Once we have grasped the basic logic of the stress colouring, we can start to enjoy the reading of combined map of stress, faults and elevations. The possibility of a relatively easy multi-contextual map reading is one of the main advantages of our stress colouring scheme — in the World Stress Map, already the stress layer alone is hardly readable.

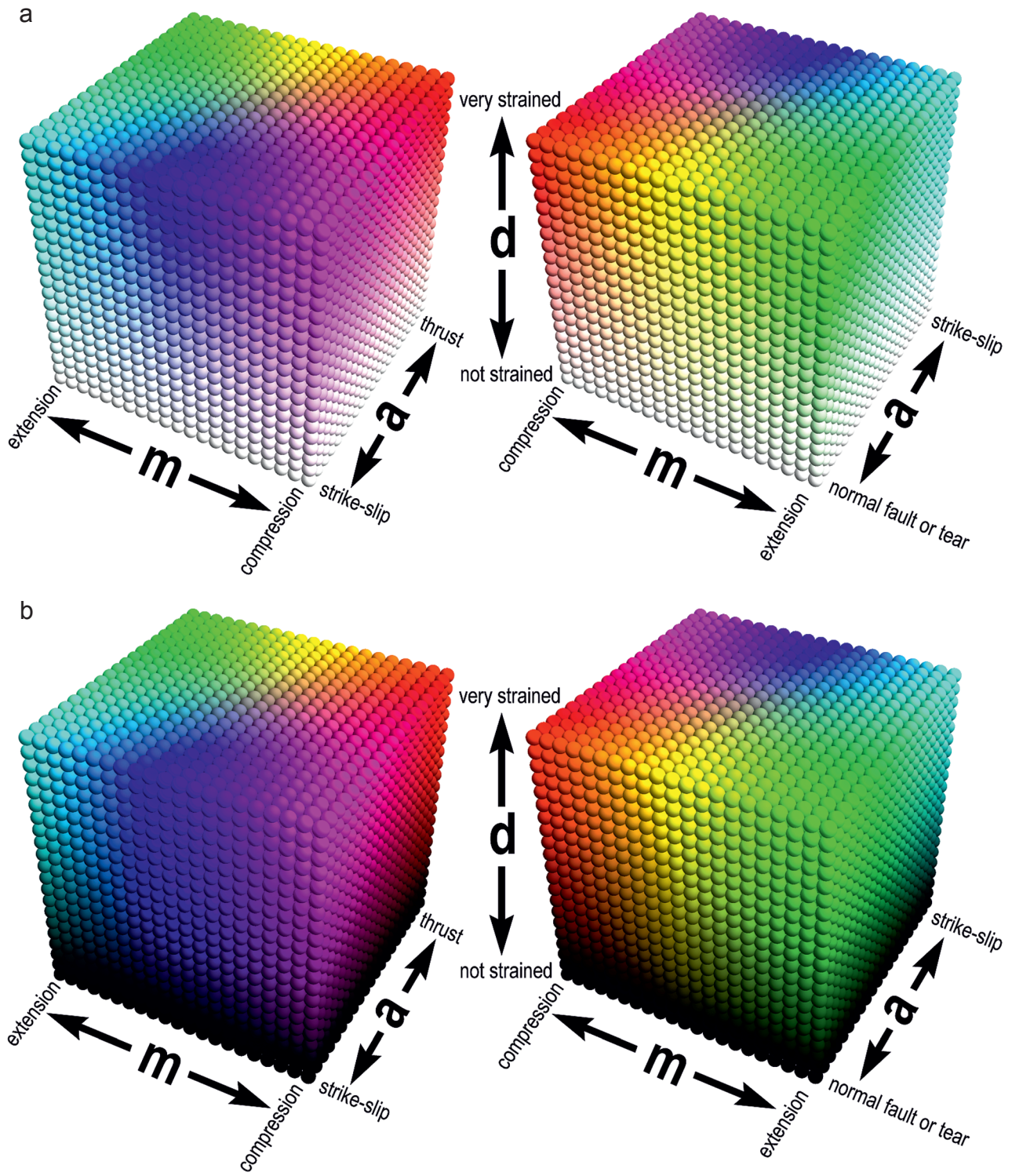

Fig. 3. a — 3D colour palette on white background (20) used for colouring the stress/strain (rate) states in front view (left) and rear view (right). **b** — 3D colour palette on black background (21) used for colouring the stress/strain (rate) states in front view (left) and rear view (right).

Let us start with a map for which we do not need any colours at all (Fig. 4). The measured velocities are fitted by a purely translational field, that generates zero strain rates. In the case of the whole-region least squares fit, the maximum approximation error was $\Delta v_y = -0.712$ mm/year in LOMS (greater than the respective standard deviation). In the case of the whole-region adaptive weights fit, the maximum approximation error was $\Delta v_y = 0.602$ mm/year in ZISE (greater than the respective standard deviation). In Fig. 4, we show only the more successful adaptive weights fit.

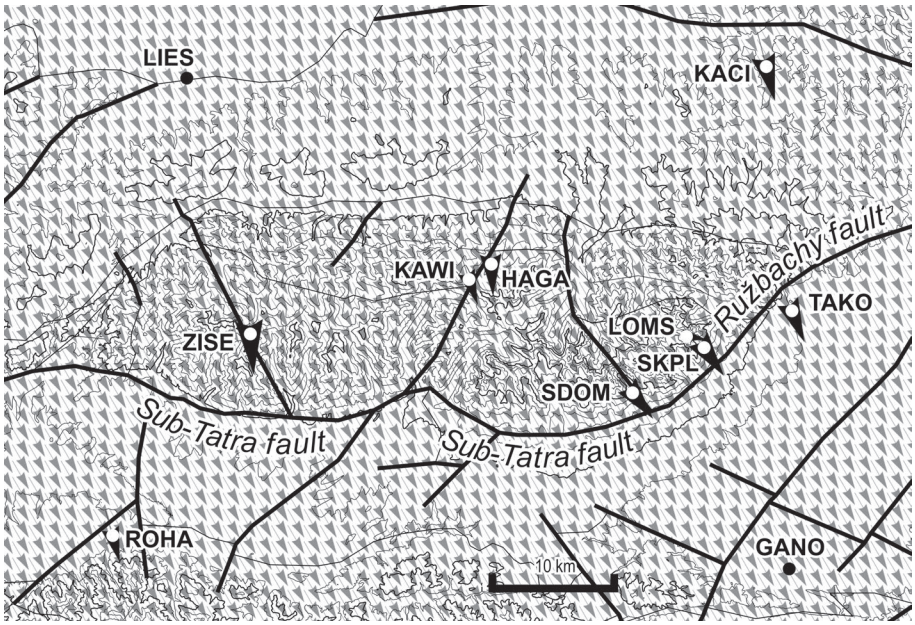

Fig. 4. Measured (black arrows) and interpolated (grey arrows) surface velocities shown together with height contours (interval 200 m) and fault scheme according to Bezák et al. (2008). The two velocity fields have different scales. Adaptive weights least squares interpolation of the 0-th order was used. The stations included in the interpolation are represented by white dots, the excluded stations by black dots.

Let us continue with the simplest possible model that generates nonzero strain rates and thus, colours different from the background. It is the bilinear velocity field ((2) for $M=1$, $N=1$). In the case of the whole-region least squares fit, the maximum approximation error was $\Delta v_y = -0.560$ mm/year in LOMS (greater than the standard deviation). In the case of the whole-region adaptive weights fit, the maximum approximation error was $\Delta v_y = 0.487$ mm/year in TAKO (slightly smaller than the standard deviation).

We see that the whole-region bilinear velocity field can model considerable variations of the velocity directions and in spite of that, generate a strain field, whose tensor descriptors vary only moderately. Moreover, the velocity fields that both are acceptable as the solutions of the interpolation problem generate contradictory colour maps (Fig. 5a,b).

Our preliminary conclusion from this contradiction is that on a regional scale, no relevant strains occur within the specified region of the Tatra Mts. The search for relevant strains should be focused on more detailed scales and local structures. To sharpen the lens, we have to increase the polynomial order in (2). The problem with this approach is that discarding GANO and LIES because of their unsatisfactory geological setting, we are left with 9 data points. The number of unknown coefficients of the biquadratic fit is exactly 9. The system is just-determined and has a unique solution, that is however no reason for jubilation. In this case, we no longer have a minimization problem, but in its stead an exact interpolation, that strictly adheres to the possibly unreliable values at the data points. The interpolated velocity field has a huge ratio of the largest to the smallest velocity and the velocity directions behave rather unbelievably between the data points that are close neighbours (Fig. 6a).

One — mathematically not very satisfactory — remedy would be an incomplete polynomial, that grants the fit some freedom. If we discard the highest powers term $c_{22}x^2y^2$ in the biquadratic polynomial, we get a smoother velocity and strain field (Fig. 6b). In both cases, the interpolation errors at the measurement points are so small that it makes no sense to start the iterations of the adaptive weights method.

Increasing the polynomial order in the whole-region approximation allows it, allegorically speaking, to develop "weird fantasies" on why the two data points next to each other have different velocities, because it is misadvised by very distant data points that have a very distant idea about the true relationship of the former two data points.

Therefore, the distant data points should not be taken as seriously as the data points next to the interpolation point. This is the main idea behind the moving least squares method. Because of the locally valid fit of the data, we label it as a local interpolation, in contrast to the whole-region interpolation. As a matter of fact, the moving least squares method in the implementation of Pohánka (2005) takes into account the complete set of data points just as the whole-region methods, but for each interpolation point, it generates its own interpolation formula, valid only at that single point.

The results of the moving least squares (Fig. 7b) are in good accordance with the biquadratic whole region fits (Fig. 6a,b). Obviously, only after going into the second polynomial order and into the local scales, the interpolation methods are able to focus on the Sub-Tatra fault system and parallel structures, whose motions were averaged out in the bilinear whole region fit.

For the reasons of the dependence of the colourable a on d and m and also because of the palette saturated in those maps, where we had to ignore the extreme strain artefacts at the margins of the region, the colours generated by our method resemble pure spectral colours. This is an advantage that can be used in the diagnostics of differences between two (or more) maps: where very different colours are superimposed onto each other, the resulting blend is a dirty, khaki colour that can be easily recognized in the compound map. To assure the fairness of the comparison, all the palette range settings in all thus compared maps have to be the same.

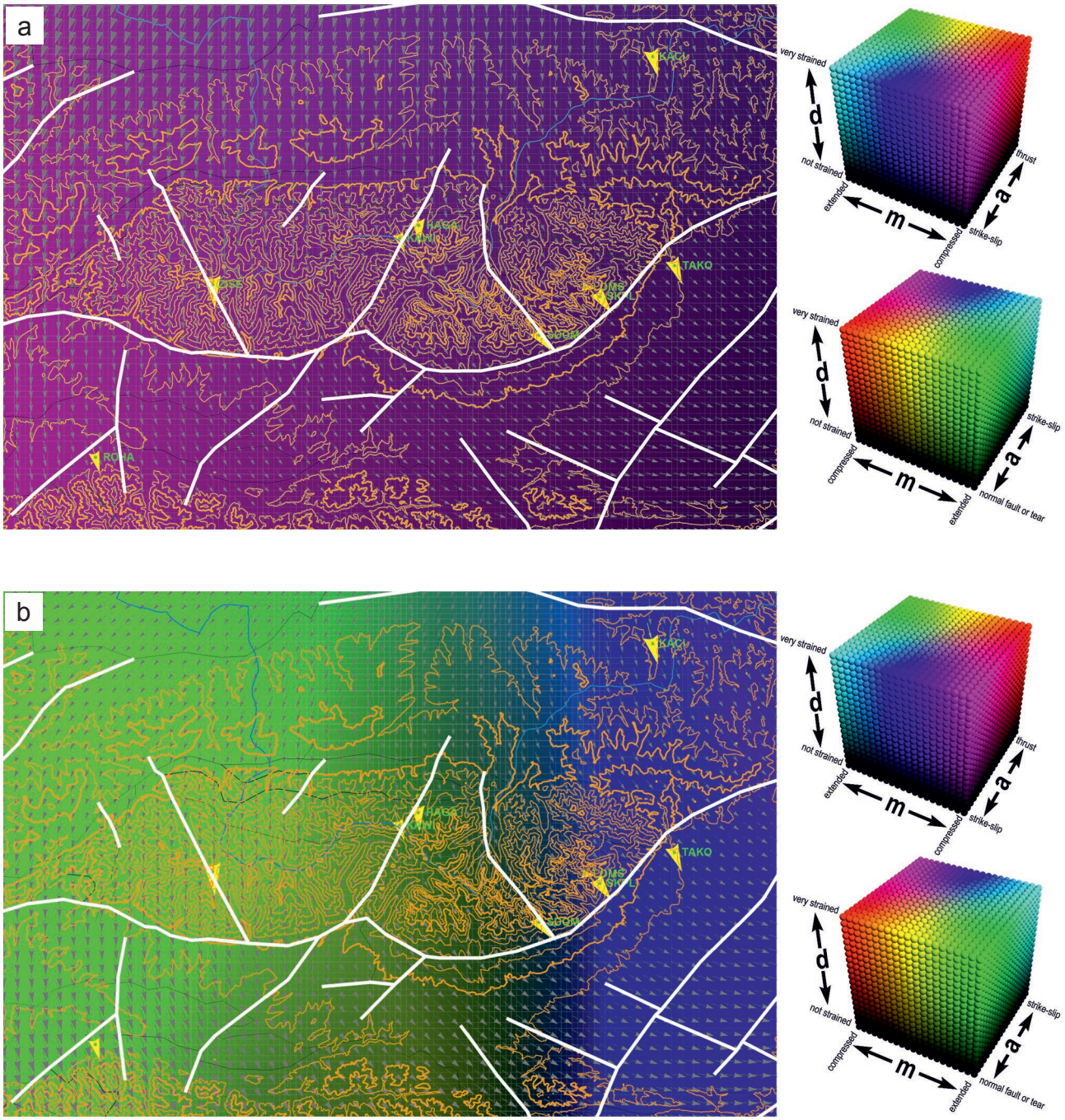

Fig. 5. Strain rate colour map, measured (yellow arrows) and interpolated (grey arrows) surface velocities shown together with height contours (in orange, interval 200 m) and fault scheme according to Bezák et al. (2008). The two velocity fields have different scales.
a — Whole-region least-squares bilinear interpolation was used. The vertices of the black background palette ((21), Fig. 3b) correspond to D_{min}=15 nstrain/year, D_{max}=20 nstrain/year, M_{min}=–5 nstrain/year, M_{max}=5 nstrain/year, A^{log}_{min}=–1.74, A^{log}_{max}=1.74 (logarithmic scale (16) with b=2 used). A part of the *D, M, A* triplets comes out of the specified range and is projected onto the surface of the palette cube (palette saturation).
b — Whole-region adaptive weights least-squares bilinear interpolation was used. The vertices of the black background palette ((21), Fig. 3b) correspond to D_{min}=0 nstrain/year, D_{max}=20 nstrain/year, M_{min}=–20 nstrain/year, M_{max}=20 nstrain/year, A^{log}_{min}=–1.27, A^{log}_{max}=1.27 (logarithmic scale (16) with b=2 used). A part of the *D, M, A* triplets comes out of the specified range and is projected onto the surface of the palette cube (palette saturation).

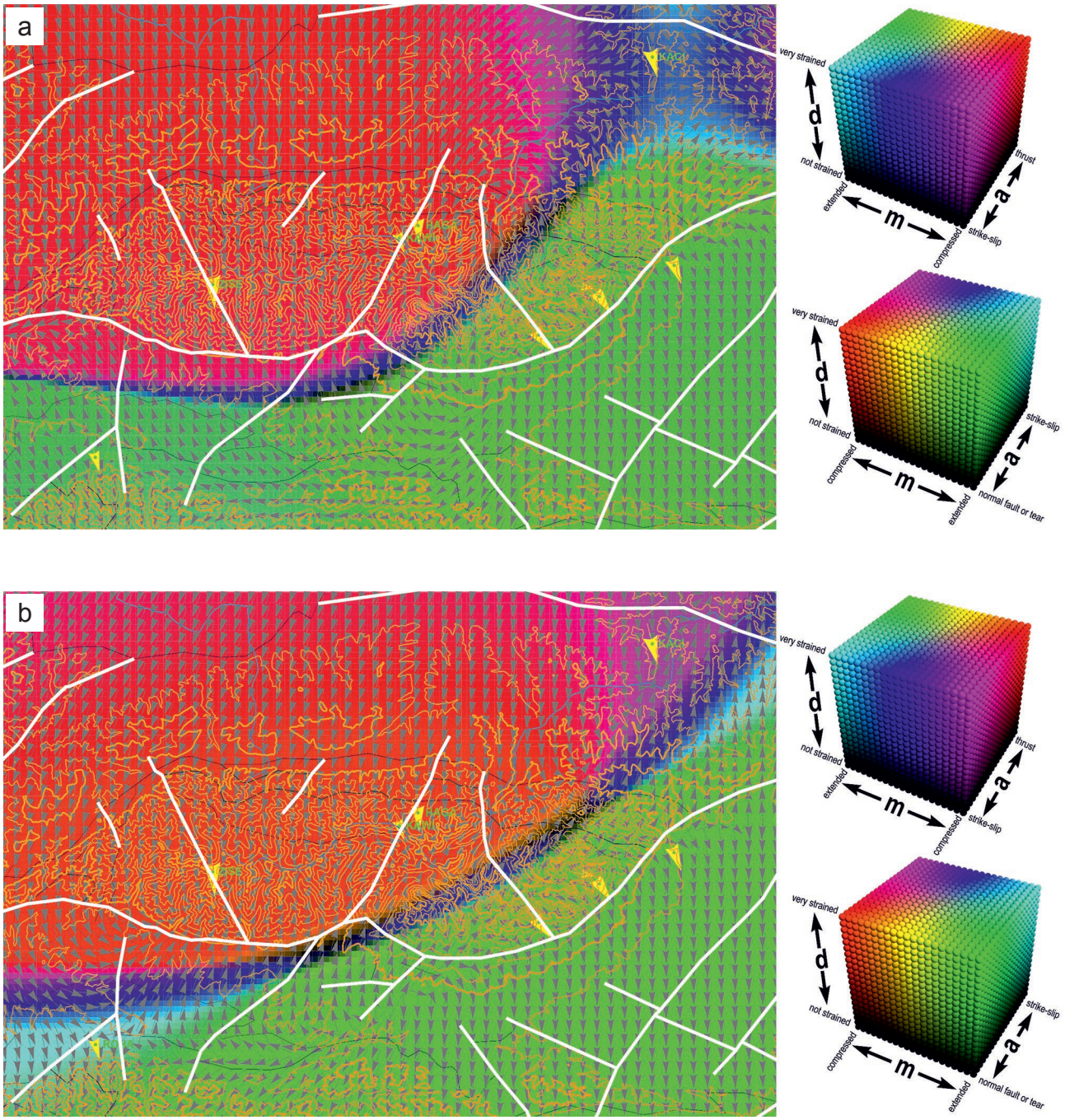

Fig. 6. Strain rate colour map, measured surface velocities (yellow arrows) and interpolated surface velocity directions (grey arrows) shown together with height contours (in orange, interval 200 m) and fault scheme according to Bezák et al. (2008).
a — Whole-region least-squares fully biquadratic interpolation was used. The vertices of the black background palette ((21), Fig. 3b) correspond to $D_{\min}=0$ nstrain/year, $D_{\max}=100$ nstrain/year, $M_{\min}=-100$ nstrain/year, $M_{\max}=100$ nstrain/year, $A^{\log}_{\min}=-1.22$, $A^{\log}_{\max}=1.22$ (logarithmic scale (16) with $b=2$ used). A considerable part of the *D, M, A* triplets (mainly at the region's margins) comes out of the specified range and is projected onto the surface of the palette cube (palette saturation).
b — Whole-region least-squares incomplete biquadratic interpolation was used. The vertices of the black background palette ((21), Fig. 3b) correspond to $D_{min}=0$ nstrain/year, $D_{max}=100$ nstrain/year, $M_{min}=-100$ nstrain/year, $M_{max}=100$ nstrain/year, $A^{\log}_{\min}=-0.422$, $A^{\log}_{\max}=0.422$ (logarithmic scale (16) with $b=2$ used). A considerable part of the *D, M, A* triplets (mainly at the region's margins) comes out of the specified range and is projected onto the surface of the palette cube (palette saturation).

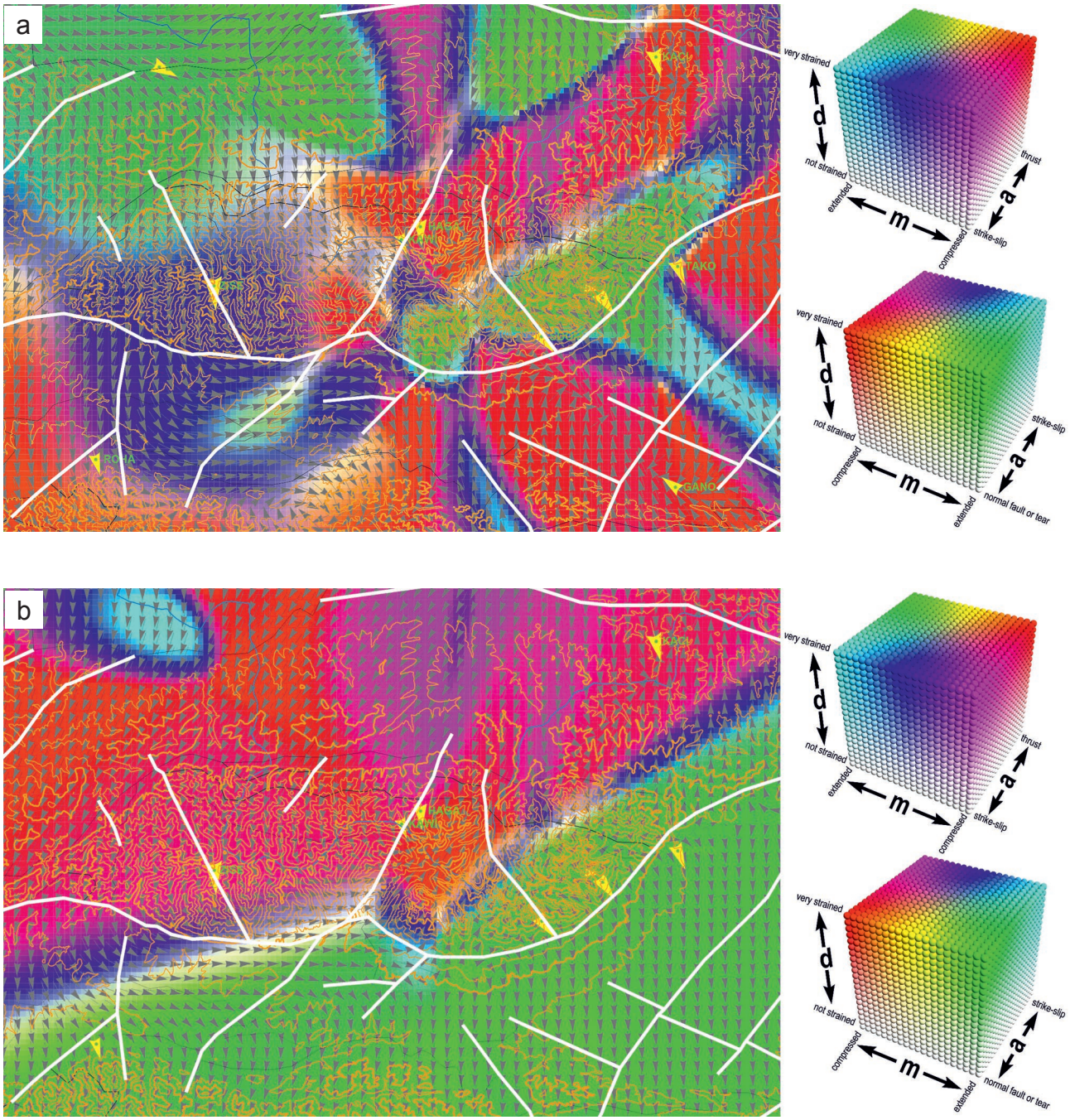

Fig. 7. Strain rate colour map, measured surface velocities (yellow arrows) and interpolated surface velocity directions (grey arrows) shown together with height contours (in orange, interval 200 m) and fault scheme according to Bezák et al. (2008).
a — Moving least-squares interpolation (smoothing distance d_0=10 km, regularization distance d_1=320 km) was used with all 11 stations involved. The vertices of the white background palette ((20), Fig. 3a) correspond to D_{min}=0 nstrain/year, D_{max}=100 nstrain/year, M_{min}=−100 nstrain/year, M_{max}=100 nstrain/year, A^{log}_{min}=−1.0, A^{log}_{max}=1.0 (logarithmic scale (16) with b=2 used). A considerable part of the *D, M, A* triplets (mainly at the region's margins) comes out of the specified range and is projected onto the surface of the palette cube (palette saturation).
b — Moving least-squares interpolation (smoothing distance d_0=10 km, regularization distance d_1=320 km) was used with 9 stations involved. The vertices of the white background palette ((20), Fig. 3a) correspond to D_{min}=0 nstrain/year, D_{max}=100 nstrain/year, M_{min}=−100 nstrain/year, M_{max}=100 nstrain/year, A^{log}_{min}=−1.0, A^{log}_{max}=1.0 (logarithmic scale (16) with b=2 used). A considerable part of the *D, M, A* triplets (mainly at the region's margins) comes out of the specified range and is projected onto the surface of the palette cube (palette saturation).

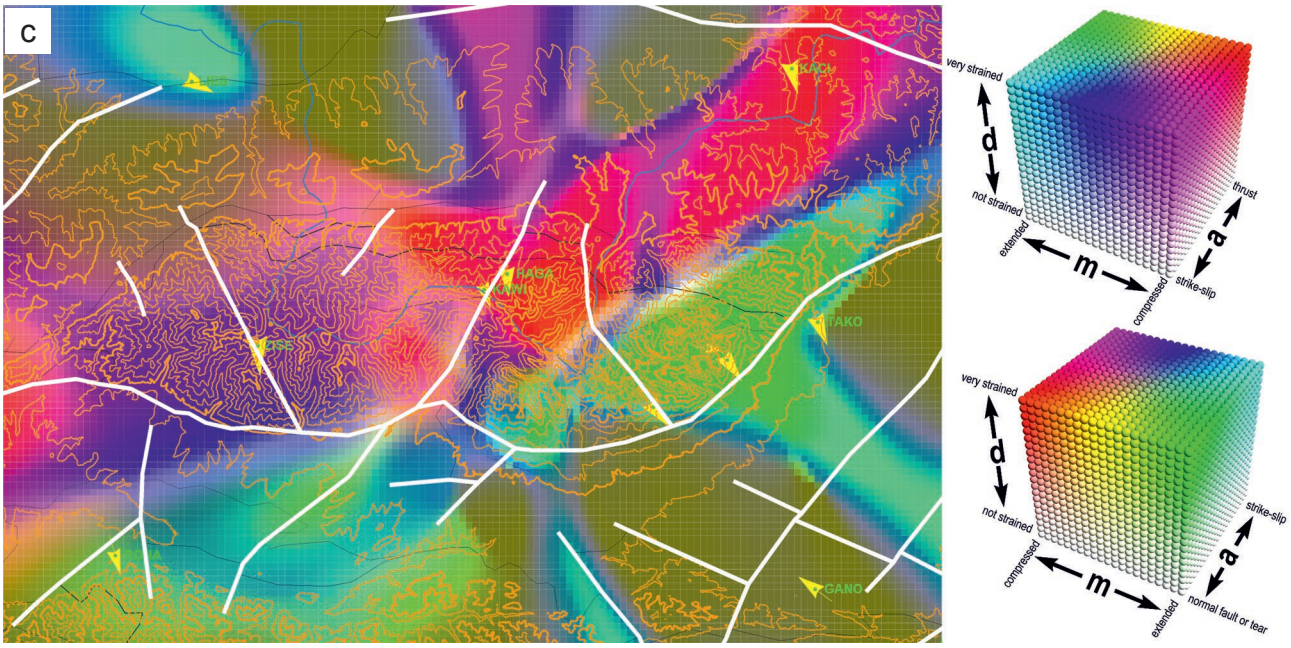

Fig. 7. c — Strain rate colour blend map and measured surface velocities (yellow arrows) shown together with height contours (in orange, interval 200 m) and fault scheme according to Bezák et al. (2008). The colour map for 11 stations (Fig. 7a) and 9 stations (Fig. 7b) were blended together. Where the maps are not in mutual agreement, colours different from the colours in (Fig. 7a, b) appear. The bigger the disagreement, the dirtier the resulting blend.

We demonstrate it on the example of two maps generated by the moving least squares interpolation. In the first one, the interpolation is based on all 11 original data points, including GANO and LIES. In the second one, the interpolation is based on 9 data points without GANO and LIES. We clearly see that the khaki spots cover not only the areas next to GANO and LIES, but all the areas insufficiently covered by data points.

Discussion

The detection of the Sub-Tatra fault system in the second order interpolation by such a low number of GNSS stations (even not deployed across the fault) is pleasant and suspicious at the same time. It may be argued that the line separating the compression and extension zone is an artefact determined by the geometry of the GNSS network rather than by the true geodynamics. Another problem is the reliability of the biquadratic approximation that does not (because it cannot) take into account the high data uncertainties. The interpolated velocity field in the band between the two groups of stations does not behave according to the natural expectations. The decision not to pay attention to the changing principal directions of strain rates and display only the tensor shape descriptors was correct, given the data uncertainties and interpolation errors visible in the interpolated velocity field.

On the other hand, we have independent evidence consistent with the extension of the southern part and compression of the northern part of the Tatra Mts. that we have found in this study. It is a known fact that the neotectonic uplift of the Tatra horst was asymmetrical, with faster uplift rates in the south and tilting down towards the north. This is the reason why the highest Tatra peaks are found southwards from the main ridge. Recently, Králiková et al. (2014) studied the tectonic evolution of the Tatra Mts. based on combined structural, sedimentary, geomorphological, and fission track data evidence. The study by Anczkiewicz et al. (2015) confirmed the asymmetry of the Tatra Mts. uplift by low-temperature thermochronology. The study by Szalaiová et al. (2008) provides a gravimetrical indication to the southward dipping of the Sub-Tatra fault.

Whereas we take for trustworthy the compression in the north and extension in the south of the Tatra Mts. computed from the GNSS data, the line between the two zones deserves some further discussion. It is parallel to the Sub-Tatra fault system. Nevertheless, if the extension and compression should be linked to the tilting of the horst, it should be rather identified with the axis of the tilt, and the Sub-Tatra fault system rather with the warm green maxima. The exact course of the two lines cannot be determined from that sparse and uncertain GNSS data.

The Sub-Tatra fault could have eased the post-glacial rebound of Tatra Mts. In this case, the strain rate pattern along the normal fault should be extensional, as well. If the faults on the northern foot of the Tatra Mts. are harder to mobilize than the Sub-Tatra fault, the uplift due to the rebound could be tilted northwards, just as the neotectonic uplift.

The orders 0, 1 and 2 of the interpolating polynomials can be interpreted as levels of trust in the surface velocity GNSS

data and, at the same time, as degrees of cartographic generalization coupled to the scale of observation.

The order 0 corresponds to the deep mistrust that us allows to interpret the GNSS data only as pure translation (although this mistrust is slightly deeper than the standard deviations of the data permit). In the resulting map, no strain/stress rates appear. In the scales of whole-world stress/strain mapping, the stress/strain rates in the region are really negligible.

The order 1 corresponds to a cautious and balanced approach to the velocities and their deviations. This order allows for considerable variations of the data within their uncertainties. The two colour maps generated from the interpolated data contradict each other. The order 1 also corresponds to the regional scale cartographic generalization, in which the local behaviour is averaged out in the regional trends. These proved insignificant, as well.

The order 2 combined with the low number of stations manifests an undue trust in the velocity means and undue ignorance of their uncertainties. On the other hand, only this and higher orders allow to focus on the local scale behaviour that got oversmoothened in the order 1 interpolation. In our application, however, the order 2 proved unable to preserve realistic regional trends alongside the local behaviour.

One viable solution we found for going into local scales was a local interpolation method – the moving least squares (Pohánka, 2005). With only 9 stations that qualified into the selection, the performance of this method was far from the optimum that would be achievable in an application with more sites more evenly distributed.

Thus, all the solutions provided by the interpolations of order 0, 1, 2 (or rather the moving least squares in the latter case) are possible answers to the question of what the GNSS data tell us about the surface deformations in the Tatra Mts. region. The reader's choice of the right answer depends on his trust in the data and on the spatial scale he is interested in.

The colour rendering of the strain rates allows an easy visual comparison of the strain rate maps generated for different parameter settings or different input data. A simple average of the RGB values in the maps efficiently displays their differences as dirty spots. The compound map would thus be automatically partitioned into subregions with different degrees of reliability. In Mentlík & Novotná (2010), the scientific reliability rating of the map content is based on an expert's assessment. Our two maps prepared by moving least squares interpolations for 11 and 9 stations are in mutual accordance mainly in the area with higher density of the stations. The rest of the region shows an instability of the interpolation solution (although exaggerated by removal of the two most problematic stations GANO and LIES). Ideally, the stations should be sufficiently numerous to ensure that removing a few of them does not change the colour map very substantially.

The colour maps averaging can be used in an effective visualization of the data uncertainties, as well. For instance, we could repeatedly generate random site velocities with the same mean and same standard deviation as in the measured dataset. For each randomly generated dataset, we could compute the colour map and finally collect the maps, average them and partition them into areas of different reliability. Alternatively, the time span of the original measurements could be split into subintervals and for each of them, a dataset of stations' short term average velocities could be computed. The evolution of the strain field and of its uncertainties in time could be animated by a sequence of individual colour maps or by adding map by map to the average compound colour map. Such an animation is, however, difficult to show in the form of a classical journal paper.

Conclusion

The horizontal surface velocities and their standard deviations at 9 or 11 stations within the Tatra Mts. region allow us to construct a broad range of interpolated velocity field solutions. The colour maps of the whole-region least squares approximations up to the polynomial order 1 show no remarkable regional trends of surface strain rates. The whole-region least squares fits by higher order polynomials are problematic not only because of the low number of data points. Thus, to resolve more local variations of the strain rates, local interpolation methods should be used. Out of them, we tested the moving least squares method and it yielded promising results. For the full deployment of the local interpolation methods' potential, more (and at the same time, more evenly distributed) local data is needed: the most welcome would be the velocities of site couples across the known faults, which are not abundant in the current dataset.

The tensor colouring method now adapted to the strain rate field at the Earth's surface proved to be a useful tool in showing the spatial variations of the relevant strain rate tensor shape descriptors in the form of colour maps. The application of the method even to a sparse dataset has clearly demonstrated its advantages: modest computational requirements, high resolution, easy intuitive readability of resulting maps, natural, easy to implement and reader-friendly colour imaging of data uncertainties, integrability into multi-contextual graphic rendering of geophysical data by standard geographical information systems.

Acknowledgements: The authors are grateful to the Slovak grant agency VEGA (grants No. 2/0002/12 , 1/0642/13, 1/0141/15, 1/0714/15, 2/0042/15, 2/0091/15) and to the Slovak Research and Development Agency (grants APVV-0724-11 and APVV-0212-12) for the partial support of this work.

References

Altamimi Z., Collilieux X., Legrand J., Garayt B. & Boucher C. 2007: ITRF2005: New release of the International Terrestrial Reference Frame based on time series of station positions and Earth Orientation Parameters. *J. Geophys. Res.* 112, B09401.

Anczkiewicz A.A., Danišík M. & Środoń J. 2015: Multiple

low-temperature thermochronology constraints on exhumation of the Tatra Mountains: New implication for the complex evolution of the Western Carpathians in the Cenozoic. *Tectonics* 34, 11, 2296–2317.

Bada G., Horváth F., Dövényi P., Szafián P., Windhoffer G. & Cloetingh S. 2007: Present-day stress field and tectonic inversion in the Pannonian basin. *Global Planet. Change* 58, 1–4: 165–180.

Bednárik M. & Kohút I. 2012: Three-dimensional colour functions for stress state visualization. *Computers & Geosciences* 48, 117–125.

Bezák V., Broska I., Ivanička J., Ivanička J., Polák M., Potfaj M., Buček J., Janočko J., Kaličiak M., Konečný V., Šimon L., Elečko M., Fordinál K., Nagy A., Maglay J. & Pristaš J. 2008: New edition of general geological map of the Slovak Republic in the scale 1:200,000 [Prehľadná geologická mapa Slovenskej republiky 1:200 000]. *Ministry of environment of the Slovak Republic, State Geological Institute of Dionýz Štúr*, Bratislava.

Bezák V., Broska I., Ivanička J., Reichwalder P., Vozár J., Polák M., Havrila M., Mello J., Biely A., Plašienka D., Kaličiak M., Žec B., Elečko M., Janočko J., Preszlényi M., Marko M., Maglay J. & Pristaš J. 2004: Tectonic map of the Slovak Republic at 1:500,000 scale [Tektonická mapa Slovenskej republiky 1:500 000]. *Ministry of environment of the Slovak Republic*, Bratislava. ISBN 80-88974-62-3 (in Slovak).

Briestenský M. & Stemberk J. 2008: Monitoring mikropohybov v jaskyniach západného Slovenska. *Acta Carsologica Slovaca*, 46, 2, 77–83.

Briestenský M. 2008: Indicators of fault activity in the Brezovské part of Malé Karpaty Mts. [Indikátory zlomovej aktivity brezovskej časti Malých Karpát]. *Geomorphologia Slovaca et Bohemica*, 8, 1, 16–25 (in Slovak).

Burchart J. 1972: Fission-track age determinations of accessory apatite from the Tatra Mountains, Poland. *Earth Planet. Sci. Lett.* 15, 4.

Czarnecki K. & Mojzeš M. 2000: Geodynamics of Tatra Mountains — present status and development of the project. *Report on geodesy* 7, Warszawa,123–124.

Dach R., Hugentobler U., Fridez P. & Meindl M. 2007: Bernese GPS Software version 5.0, Astronomical Institute, University of Bern.

Drewes H. 2009: The actual plate kinematic and crustal deformation model APKIM2005 as basis for a non-rotating ITRF. In: Geodetic reference frames. *Springer*, Berlin, 95–99.

EPN 2016: EUREF permanent network. Available online at: http://www.epncb.oma.be.

Fejes I. 2002: Consortium for Central European GPS Geodynamic Reference Network (CEGRN): Concept, Objectives and Organization. *Reports on Geodesy* 61, 1, 15–21.

Fojtíková L., Vavryčuk V., Cipciar A. & Madarás J. 2010: Focal mechanisms of micro-earthquakes in the Dobrá Voda seismoactive area in the Malé Karpaty Mts. (Little Carpathians), Slovakia. *Tectonophysics* 492, 1–4, 213–229.

Hefty J. & Gerhátová Ľ. 2006: Site velocities from long-term epoch GPS observations — Case study: Central Europe regional geodynamics project 1994–2005. *Acta Geodyn. Geomater.* 3, 3 (143), 7–17.

Hefty J. 2004: Global positioning system in 4D geodesy [Globálny polohový systém v štvorrozmernej geodézii]. *STU*, Bratislava. ISBN 80-227-2027-5, 1–112 (in Slovak).

Heidbach O., Tingay M., Barth A., Reinecker J., Kurfeß D. & Müller B. 2009: The World Stress Map based on the database release 2008, equatorial scale 1:46,000,000. *Commission for the Geological Map of the World*, Paris, doi: 10.1594/GFZ.WSM.Map2009.

Hradilek L. 1984: Alpine surveying, trigonometric leveling and 3-dimensional terrestrial triangulation [Vysokohorská geodézie — trigonometrická nivelace a trojrozměrná terestrická triangulace]. *Academia*, Praha, 1–230 (in Czech).

IGS 2016: International GNSS Service. Available online at: http://igscb.jpl.nasa.gov/.

Jarosiński M., Beekman F., Bada G. & Cloetingh S. 2006: Redistribution of recent collision push and ridge push in Central Europe: insights from FEM modeling. *Geophys. J. Int.* 167, 2, 860–880.

Košťák B. 1969: A new device for in-situ movement detection and measurement. *Experimental Mechanics* 9, 8, 374–379.

Králiková S., Vojtko R., Sliva Ľ., Minár J., Fügenschuh B., Kováč M. & Hók J. 2014. Cretaceous–Quaternary tectonic evolution of the Tatra Mts. (Western Carpathians): constraints from structural, sedimentary, geomorphic, and fission track data. *Geol. Carpath.* 65, 4, 307–326.

Littva J., Hók J. & Bella P. 2015: Cavitonics: Using caves in active tectonic studies (Western Carpathians, case study). *J. Struct. Geol.* 80, 47–56.

Mentes Gy. 2008: Observation of recent tectonic movements by extensometers in the Pannonian Basin. *J. Geodynamics* 45, 4–5, 169–177.

Mentlík P. & Novotná M. 2010: Elementary forms and "scientific reliability" as an innovative approach to geomorphological mapping. *Journal of Maps* 6, 1, 564–583.

Nemčok J., Bezák V., Biely A., Gorek A., Gross P., Halouzka R., Janák M., Kahan Š., Kotański Z., Lefeld J., Mello J., Reichwalder P., Rackowski W., Roniewicz P., Ryka W., Wieczorek J. & Zelman J. 1994: Geological map of the Tatra Mts. at 1:50,000 scale [Geologická mapa Tatier 1:50 000]. *Ministry of environment of the Slovak Republic , State Geological Institute of Dionýz Štúr, MOSZNL, PIG*, Bratislava (in Slovak).

Nemčok J., Bezák V., Janák M., Kahan Š., Ryka W., Kohút M., Lehotský I., Wieczorek J., Zelman J., Mello J., Halouzka R., Rackowski W. & Reichwalder P. 1993: Explanatory notes to the geological map of the Tatra Mts. at 1:50,000 scale [Vysvetlivky ku geologickej mape Tatier 1: 50 000]. *State Geological Institute of Dionýz Štúr*, Bratislava, 1–135 (in Slovak).

Papčo J. 2010: Monitoring of the Earth's Crust Deformations in Alpine Area [Monitorovanie deformácií zemskej kôry vo vysokohorskom prostredí]. *Thesis, Slovak University of Technology in Bratislava, Faculty of Civil Engineering*, 1–127 (in Slovak, with English summary).

Pohánka V. 2005: Universal interpolation method for many-dimensional spaces. Available online at: http://gpi.savba.sk/GPIweb/ogg/pohanka/int.pdf.

Sperner B. & Ratschbacher L. 1995: Rise and fall of the High Tatra Mts. In: Proceedings of Europrobe Workshop Pancardi. *SAV*, Bratislava, 67–69.

Stangl G. 2007: Guidelines for CEGRN Reprocessing version 1.3. Available online at: http://cergops2.iwf.oeaw.ac.at.

Szalaiová E., Bielik M., Makarenko I., Legostaeva O., Hók J., Starostenko V., Šujan M. & Šefara J. 2008: Calculation of a stripped gravity map with a high degree ofaccuracy: a case study of Liptovská Kotlina Basin (Northern Slovakia). *Geol. Quarterly* 52, 2, 103–114.

Appendix

Surface deformation velocity in Tatra Mountains region — source data by Papčo (2010)

#	code	X_east_UTM [m]	Y_north_UTM [m]	Z [m]	DY_north [m/year]	SDY [mm/year]	DX_east [m/year]	SDX [mm/year]	DZ_vertical [m/year]	SDZ_vertical [mm/year]
7	GANO	450554.732	5431524.174	701.17	0.00049	0.35	–0.00067	0.28	0.0014	2.16
9	HAGA	427582.955	5454992.094	1530.04	–0.00094	0.45	5.00E–05	0.34	–0.00069	2.59
11	KACI	448794.152	5470266.647	553.68	–0.00102	0.38	0.00026	0.3	–0.0018	2.26
18	KAWI	425866.824	5453835.261	1983.40	–0.00074	0.36	0.00025	0.27	–0.00058	2.13
12	LIES	404054.365	5469346.882	692.45	–0.00046	0.35	0.00089	0.26	0.00017	2.04
13	LOMS	442665.23	5449447.723	2634.03	–8.00E–05	0.36	0.00055	0.27	–0.00184	2.16
6	ROHA	398341.867	5434026.968	736.68	–0.00076	0.33	0.00021	0.25	–0.00071	1.90
15	SDOM	438492.561	5445087.551	1675.03	–0.00077	0.46	0.0006	0.35	0.0009	2.69
16	SKPL	443989.232	5448586.154	1772.47	–0.00084	0.35	0.00059	0.27	0.00044	2.18
22	TAKO	450764.513	5451388.624	820.29	–0.00091	0.62	0.00037	0.45	0.00123	3.51
19	ZISE	408976.34	5449663.668	1916.18	–0.00121	0.41	0.0001	0.31	–0.00124	2.25